Met. Mater. Int., Vol. 18, No. 2 (2012), pp. 361~369
doi: 10.1007/s12540-012-2023-5 Published 27 April 2012

A New Method to Determine Trace Boron Concentration of Iron and Steel by SIMS Direct Ion Image

JaeNam Kim*, SangUp Lee, HyeogDae Kwun, JoonWon Kim, KwangSoo Shin, and JungJu Lee

Research Institute of Industrial Science and Technology (RIST),
Center for Analysis and Assessment, Pohang 790-330, Korea

(received date: 19 April 2011 / accepted date: 7 June 2011)

Boron is often used as a trace additive in steel in order to control the phase transformation behaviors and improve the interfacial cohesion. The aim of this work is to suggest a method to determine the trace boron concentration of iron and steel by direct ion image. The optimum conditions for direct ion imaging were proposed by means of secondary ion mass spectrometry - resistive anode encorder (SIMS-RAE). A method of quantification was examined using standard reference materials, electrolytic iron, high carbon steel, Cr-V steel and stainless steel. For the best secondary ionization efficiency, O_2^+ ion bombardment and negative secondary ion collection were used. The cluster ions of $^{11}B^{16}O_2$ and $^{56}Fe^{16}O$ were detected and processed to reduce the strong matrix effect. Every pixel, P(i, j) of 50 images was integrated and converted to a retrospective depth profile by calculator and profiler. The calibration curve and relative sensitivity factor (RSF) approach were considered. Furthermore, reproducibility of the SIMS data depending on the analytical mode was examined.

Key words: alloys, casting, surface, secondary ion mass spectroscopy (SIMS), quantification

1. INTRODUCTION

Secondary ion mass spectrometry (SIMS) microscopy is capable of providing direct mass filtered 2D or 3D ion images of materials. The SIMS microscopy technique utilizes a broad beam of primary ions to bombard the sample surface, resulting in reduced beam damage and also fast image acquisition time [1]. A spatial resolution of ≥1 μm and a depth resolution of <1 nm can be obtained in the field of view of 150 μm in the direct ion image mode.

A resistive anode encoder (RAE) is a position sensitive detector comprising a dual micro channel plate and resistive film coated on a ceramic plate. The main advantage of the SIMS microscopy with RAE is its excellent sensitivity and digitized pixel-by-pixel direct ion image data.

Another alternative for recording an image is the SIMS microprobe mode. In this mode, the primary beam is focused down to a small spot and scanned across the sample surface. The raster area is synchronized to the CRT monitor by modulating the intensity of the spot as a function of the secondary ion intensity of each position. It can be operated under maximum transmission because the largest contrast aperture is used in the microprobe mode. Biological and organic applications are the recent areas of increasing interest in quantification using time-of-flight (TOF) SIMS microscopy. For instance, relative quantification of TOF-SIMS imaging was applied to compare the level of cholesterol in cells [2] and it was suggested that the principle component analysis (PCA) and multivariate curve analysis (MCS) are the suitable quantification method for TOF-SIMS image data sets of immiscible polymer blends [3].

The role of the addition of trace boron in steels was well established [4-6] by the fact that boron increased the bainitic hardenability by retarding the heterogeneous nucleation of ferrite at the austenite grain boundary. It is considered that this effect is due to the reduction in interfacial energy, as boron segregates to the grain boundaries. The amount of soluble boron concentration which affected the incubation time for the allotriomorphic ferrite reaction has been investigated [7], and its result showed about 20 weight ppm. An excess of added boron is detrimental because it leads to the formation of borides at the austenite grain boundaries, and they are known to enhance the nucleation of ferrite. Boron oxides or nitrides are not effective for the ferrite transformation.

The matrix effect is the most serious problem in SIMS quantification. Therefore, the sample is analyzed together with calibration standards which contain chemical composition and matrices close to the requirements. However, it is not possible to set all combinations of chemical composition and matrices. Hence, the quantification of SIMS micros-

*Corresponding author: jnkims@rist.re.kr
©KIM and Springer

copy in the field of metallurgy has so far not been utilized much. In spite of its difficulty in quantification for iron and steel samples, the SIMS direct ion imaging mode is still a quite interesting tool to record the boron distribution in the range of ~ ppm, about 10 times faster than the SIMS microprobe mode (scanning mode). Typically, the SIMS microprobe mode needs more than 30 minutes for one frame of elemental map but several minutes for SIMS microscope mode (RAE image). It has been discussed that the SIMS raster in-depth profile analysis of steel samples is complicated [8]. SIMS depth profile of steel is likely to meet many difficulties because of the possibilities of encountering rough surface, multiple phases, grain boundaries, inclusions, precipitates, impurities, and poly crystal orientation in the material's microstructure [9]. These possibilities may produce the loss of depth resolution and cause the matrix effect.

In this study, the RAE ion imaging technique was examined in an attempt to propose a method to determine trace boron concentration with the minimum number of standard samples, with the optimum conditions for the best ion image. A calibration curve and relative sensitivity factor (RSF) were used for quantifying the complex matrix of iron and steel. In addition, the reliability of the acquisitions was also discussed.

2. EXPERIMENTAL PROCEDURES

The minimum number of standard reference materials was selected in this study. They are four standards of Cr-V steel (SRM 1263a-NIST), high carbon steel (SRM 1264a-NIST), electrolytic iron (SRM 1265a-NIST), and stainless steel (SRM C1151a-NIST). The chemical composition of the test samples is listed in Table 1. The value listed in Table 1 is not expected to deviate from the true value by more than ±1 in the last significant figure reported. For a subscript figure, the deviation is not expected to be more than ±5 according to the certification sheet. The subscript $_{NC}$ is not a certified value due to the piece to piece variability. Test samples with an area of 8×8 mm^2 and a thickness of < 5 mm were machined with a flat surface, and mirror-polished. Chemical etching was performed to observe the microstructures of the four test samples by optical microscope. Figure 1 shows the microstructures, revealing the mixture of cementite and pearlite structures for the Cr-V steel and high carbon steel, the pure ferrite phase in electrolytic iron, and the austenite phase in high chromium stainless steel, respectively. The Brinell hardness value varies depending on the phase. The cementite has the highest value of about 800 HB and the ferrite (α phase) has the lowest value of about 100HB. After the observation of microstructures, all the samples were mirror- polished again for the SIMS microscopy measurements.

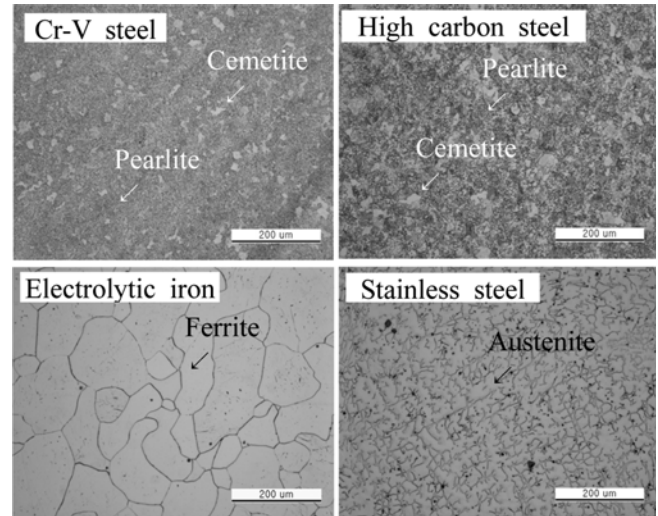

Fig. 1. Optical micrographs of the test samples. They show distinctive matrix structures.

The direct ion image in SIMS microscopy mode was acquired using RAE with CAMECA IMS 6F instrument. The experimental conditions are summarized in Table 2. In this study, the cluster ions of impurity ion species, I_i, $^{11}B^{16}O_2$, and the matrix ion species, I_m, $^{56}Fe^{16}O$ were used for RAE ion imaging because of their high detection sensitivity, compared to the single atomic ions of ^{11}B and ^{56}Fe. More-

Table 2. Experimental conditions

Item	Direct ion image	Raster depth profile
Primary ion species	O_2^+	← same
Primary beam energy	12.5kV	← same
Secondary beam energy	–4.5kV	← same
Primary beam current	1E-7A	← same
Detected ion species	I_i:$^{11}B^{16}O_2$ I_m:$^{56}Fe^{16}O$	← same
Field of view	150 μm	63 μm
Mass resolution (M/ΔM)	2,000	4,500
Counting time/Waiting time (second)	$^{11}B^{16}O_2$: 1.67/0.56 $^{56}Fe^{16}O$: 1.67/1.67	$^{11}B^{16}O_2$: 0.993/1.006 $^{56}Fe^{16}O$: 0.993/1.006
Number of points (map)	(50)	75

Table 1. Chemical composition of the test samples (wt%)

Sample	C	Si	Mn	P	S	Ni	Cr	Al	B	Fe
Cr-V steel (SRM 1263a)	0.62_6	0.74	1.50	0.02_9	0.005_7	0.32	1.31	0.24	0.0009_1	bal.
High carbon steel (SRM 1264a)	0.871	0.06_6	0.25_8	0.010	0.025	0.14	0.06_6	–	0.011_{NC}	bal.
Electrolytic iron (SRM 1265a)	0.0067	0.008_0	0.0057	0.011	0.0055	0.041	0.007_2	0.0007	0.00013	bal.
Stainless steel (SRM C1151a)	0.034	0.29	2.37	0.017	0.038	7.25	22.59	0.003_{NC}	0.001_{NC}	bal.

over, the selection of cluster ions was made with the aim of decreasing the matrix effect significantly. Mass resolution (M/ΔM) was set to 2,000 in order to eliminate the mass interference between cluster ion and the specific element ion. The L3 lens voltage of the spectrometer should be set to zero during direct ion image mode and the L2 lens voltage was adjusted to get the constant stable primary beam current, I_p of 100 nA.

For the best image resolution, it was necessary to set the contrast aperture at the smallest size. Astigmatism from apertures and slits should be avoided during all the measurements. A field of view of 150 μm diameter was used to display the distribution of impurity species properly. Counting time for each mass was 1.67 seconds and waiting time was 0.56 seconds for $^{11}B^{16}O_2$, and 1.67 seconds for $^{56}Fe^{16}O$. A reasonable waiting time is required after each mass peak switch before starting the secondary ion intensity measurement. A total of 50 cycles of image plane were stored for one map, which was taken in about 3.3 minutes.

3. RESULTS AND DISCUSSION

3.1. Direct 2D and 3D ion imaging

It is well known that native oxide can develop instantly after a fresh surface is exposed to the air, and reach the eventual thickness of up to several nanometers, in the case of steel samples. This surface oxide layer will induce surface peaks from many species related with airborne molecular contamination [10]. The surface peak could be observed as shown in Fig. 2(C), which was a retrospective depth profile of (A) $^{11}B^{16}O_2$ and (B) $^{56}Fe^{16}O$ from the RAE ion image of the high carbon steel sample. The highest secondary ion counts of $^{11}B^{16}O_2$ and $^{56}Fe^{16}O$ found were 43,800 cps and 67,600 cps, respectively, at the top surface region. They were caused by the secondary ion yield enhancement mainly due to the oxygen in the surface oxide. The steady-state equilibrium of the secondary ions could be established after 300 seconds of surface oxide removal by pre-sputtering. The direct ion images in Fig. 3(A) and (B) show the distribution of $^{11}B^{16}O_2$ and $^{56}Fe^{16}O$ for high carbon steel. Figure 3 (C) demonstrates the nearly constant intensities of $^{11}B^{16}O_2$ and $^{56}Fe^{16}O$ secondary ion counts at the equilibrium region. The average intensities were 5,300 cps for $^{11}B^{16}O_2$ and 2,750 cps for $^{56}Fe^{16}O$, respectively. It was found that an oxygen-covered sample surface tremendously stimulated the secondary negative cluster ion emission of the steel sample, compared to its equilibrium intensity, by a factor of 8.3 for $^{11}B^{16}O_2$ and by a factor of 24.6 for $^{56}Fe^{16}O$, respectively. A general tendency to build up a negative secondary ion of ^{11}B in comparison with that of ^{56}Fe is much easier to under-

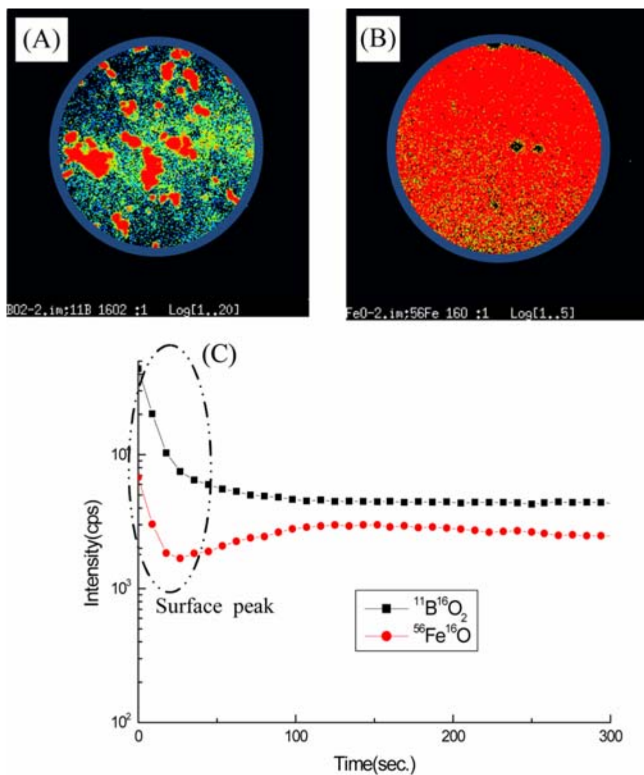

Fig. 2. Direct ion images of (A) $^{11}B^{16}O_2$ and (B) $^{56}Fe^{16}O$ acquired from as-received surface to inner side of sample for high carbon steel. (C) is the retrospective depth profile of $^{11}B^{16}O_2$ and $^{56}Fe^{16}O$ from (A) and (B).

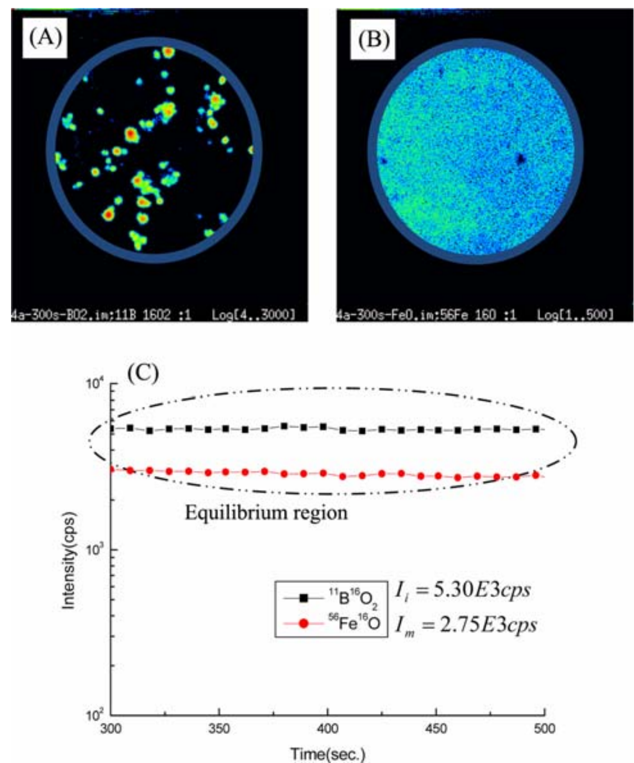

Fig. 3. Direct ion images of (A) $^{11}B^{16}O_2$ and (B) $^{56}Fe^{16}O$ acquired after 300 seconds of sputter removal of the surface contamination for high carbon steel. (C) is the retrospective depth profile of $^{11}B^{16}O_2$ and $^{56}Fe^{16}O$ from (A) and (B).

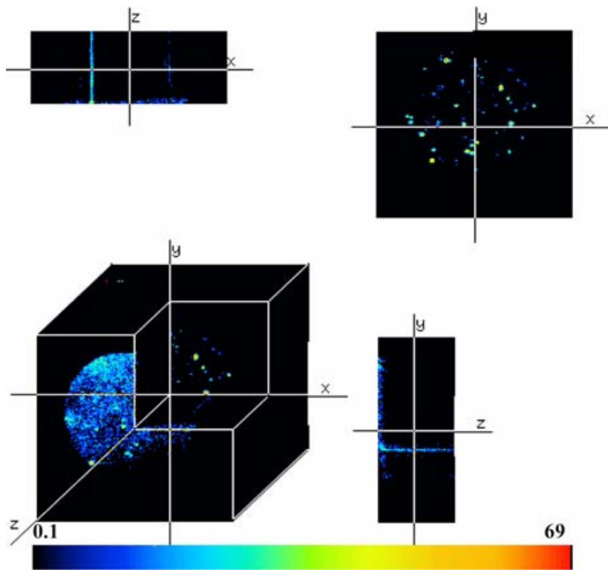

Fig. 4. Direct 3D $^{11}B^{16}O_2$ ion image of high carbon steel.

stand given the fact that the electron affinity of the negative secondary single atom ion ^{11}B (0.28 eV) is higher than that of ^{56}Fe (0.16 eV). Figure 4 shows the brighter area on the top surface corresponding to the surface oxide. The signal of the inner side is directly associated with the boron location. It can be seen that the boron has an in-homogeneous distribution to a certain extent along the depth of the sample from the top view, side view, and rear view, respectively.

3.2 Determination of trace boron concentration

In quantitative SIMS analysis, there exists some difficulty in calculating absolute atomic concentrations for all elements in the sample. It is mainly the extraction of total secondary ion currents stemming from not only single or cluster ions but also possible interferences with secondary ion peaks from other species of the different sample matrix. Hence it is important to use high mass resolution to properly extract the secondary ion current for the measurement of trace boron concentration from SIMS image data. The test samples contain a certain amount of aluminum, except the high carbon steel. Thus $^{11}B^{16}O_2$ interferes with $^{27}Al^{16}O$ in the secondary ion peak of mass 43. The former has the mass of 42.99911 and the latter 42.97645, respectively. In principle, ΔM between the 2 species is 0.02266, and therefore M/ΔM should be better than 1,897.6 for the uninterrupted detection of $^{11}B^{16}O_2$. Otherwise the quantified boron concentration includes a corresponding amount of interfering aluminum.

The matrix effect can be described as the difference in sensitivity for a given element in a sample of a different compound. The change of matrix can contribute to the ionization efficiency and sputtering yield. Therefore, a series of calibration standard samples must be used in SIMS quantitative analysis for an iron and steel sample. However, it is difficult to set all calibration standard samples for every requirement of composition and microstructure. The use of secondary cluster ion emission might be an important idea for reducing the matrix effect, even though the theoretical emission model is not well understood.

In this study, the approach to determine the trace boron concentration from the RAE-2D ion image is as follows.

a) Removal of surface oxide by 300 seconds sputtering prior to running the direct ion image.

b) Confirm the primary ion current, I_p of 100 at every stage of acquisition.

c) Acquire two RAE-2D ion images (MR 2,000) using I_i, of $^{11}B^{16}O_2$, and I_m of $^{56}Fe^{16}O$ for 50 cycles, respectively.

d) Convert every pixel of the images, $P_n(i, j)$ to count per seconds (retrospective depth profile).

e) Measure the secondary ion ratio of $^{11}B^{16}O_2/^{56}Fe^{16}O$ for all test samples.

f) Obtain the calibration curve for quantification and correlation coefficient by least square fitting.

g) Compare the standard deviation of the RSF for boron and carbon.

The information of the direct image was computed by the profiler as plotted in graph by intensity versus time, as shown in Fig. 3(C) and Fig. 5(A), (B), (C). For a given species, the intensity for each data point of the profile was computed according to the following relationship,

$$I(t_n) = \frac{\sum_{i,j} P_n(i,j)}{T} \quad (1)$$

where $P_n(i, j)$ is the pixel intensity in counts included in the contour for the *n-th* image planes, T is the integration time for each image, and t_n is the total time spent measuring from the beginning of the analysis to the end of the acquisition of the n image planes. There are several models to calculate the fractional atomic concentration of element from a measurement of sputtered ion currents. In this study, the calibration curve method was applied to the quantification of trace boron. Furthermore, the variation of RSF was calculated, to make sure of its constancy as a function of concentration under different conditions. Again note that a series of samples containing different concentrations of boron should be as similar as possible in matrix composition and microstructure.

3.2.1. Calibration curve

Retrospective depth profiles are shown in Fig. 3(C) for high carbon steel, and in Fig. 5 for (A) Cr-V steel (SRM 1263a), (B) electrolytic iron (SRM 1265a), and (C) stainless steel (SRM 1151a), respectively. The equilibrium secondary ion intensities of the impurity $^{11}B^{16}O_2$ and matrix $^{56}Fe^{16}O$ are summarized in Table 3. Figure 7 is the calibration curve with boron concentration versus the correspond-

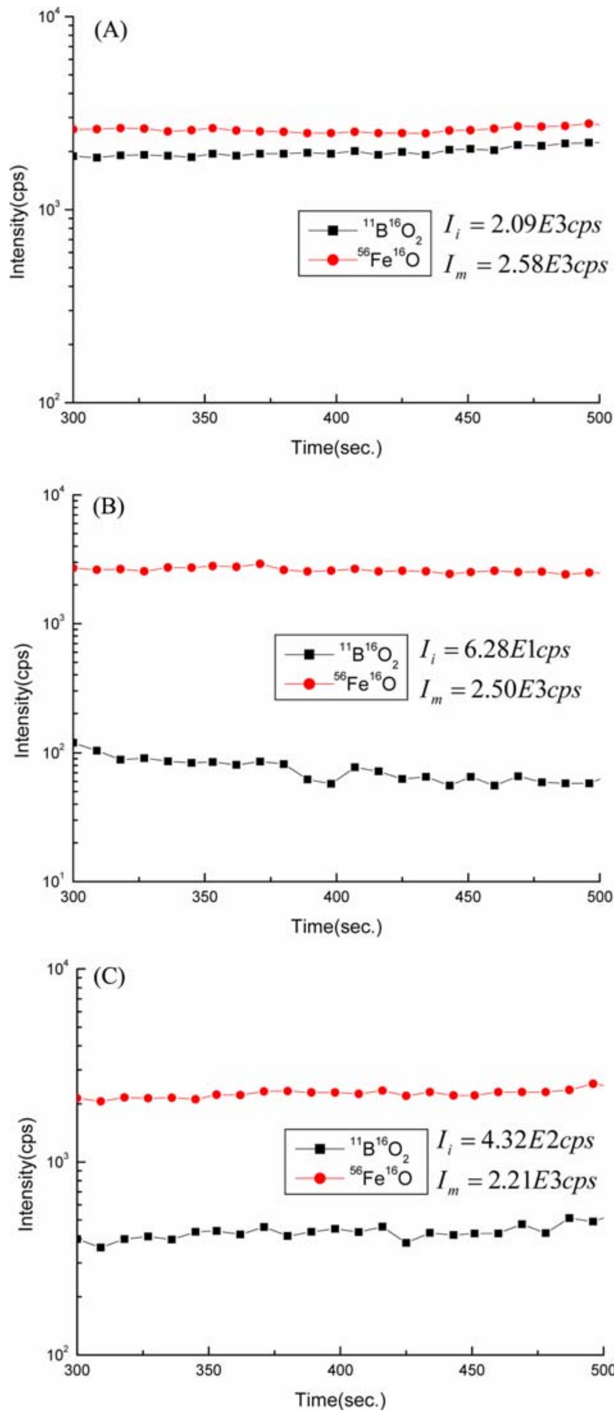

Fig. 5. Retrospective depth profiles of $^{11}B^{16}O_2$ and $^{56}Fe^{16}O$ for (A) Cr-V steel, (B) electrolytic iron, and (C) stainless steel, respectively.

ing cluster ion intensity ratio of $^{11}B^{16}O_2/^{56}Fe^{16}O$, obtained by the use of mass resolution 2,000. Two straight lines (A and B) are drawn by linear fitting using Origin 6.0 software with the fit curve options of 95 confidence, 20 points, 15 range margin, and 1 fixed slope. The red solid line "A" fitted all four test samples and the black broken line "B" fitted three test samples, except the outlier. Correlation coefficients, R are 0.9349 for fit "A" and 0.9999 for fit "B", respectively.

The outlier of the Fit "A" was identified as Cr-V steel. The amount of boron concentration of Cr-V steel (9 ppm) is close to the stainless steel (10 ppm) but the secondary ion intensity ratio of impurity $^{11}B^{16}O_2$/matrix $^{56}Fe^{16}O$ is 0.81 (Cr-V steel) and 0.195 (Stainless steel). The ratio of Cr-V steel is four times higher than that of stainless steel. One of the possible reasons for this might be the interference with the aluminum at mass 43. As mentioned before, ΔM between $^{11}B^{16}O_2$ and $^{27}Al^{16}O$ is 0.02266, and therefore M/ΔM should be better than 1,897.6 for the accurate detection of $^{11}B^{16}O_2$. Cr-V steel contains 0.24% of aluminum which is at least 30 times higher than those of other test samples; for instance, high carbon steel contains 0.008% of aluminum. High mass resolution is required to reduce the influence of the aluminum interference for the good quantification of these steel samples. But, the mass resolution of 2,000 is a critical value for the trace boron RAE ion imaging because the mass resolution better than 2,000 will lead to shadow-off the field of view in the RAE ion image (see Fig. 6). In order to prove this presumption, the raster depth profile using a mass resolution of 4,500 was examined and the corresponding calibration curve (Fig. 8) was compared with that by retrospective depth profile (Fig. 7).

Figure 8 shows the calibration curve using the mass resolution of 4,500. Two straight lines (A and B) are drawn by linear fitting like Fig. 7. The correlation coefficient of the calibration curve is improved from 0.9349 to 0.9965 for fit "A" by the use of high mass resolution. This result can confirm that the aluminum interference has an influence on the secondary cluster, $^{11}B^{16}O_2$ ion intensity. However, in the typical range of aluminum content of the samples such as high carbon steel, electric iron and stainless steel, it was demonstrated that the aluminum didn't affect the secondary cluster ion intensity of $^{11}B^{16}O_2$, leading to the very good correlation coefficient of 0.9999 with either the mass resolution of 2,000 or 4,500. The typical range of this alumi-

Table 3. Comparison of secondary ion ratio of B cluster ion and Fe cluster ion between retrospective depth profile and raster depth profile

Test Sample (Matrix)	Retrospective depth profile (MR 2,000)			Raster depth profile (MR 4,500)		
	$I_{^{11}B^{16}O_2}$ (cps)	$I_{^{56}Fe^{16}O}$ (cps)	I_i/I_m	$I_{^{11}B^{16}O_2}$ (cps)	$I_{^{56}Fe^{16}O}$ (cps)	I_i/I_m
Cr-V steel	2.09E3	2.58E3	0.81	5.08E3	1.44E4	0.352
High carbon steel	5.30E3	2.75E3	1.93	2.40E4	1.14E4	2.1
Electrolytic iron	6.28E1	2.50E3	0.025	3.57E2	1.34E4	0.026
Stainless steel	4.32E2	2.21E3	0.195	1.34E3	6.07E3	0.221

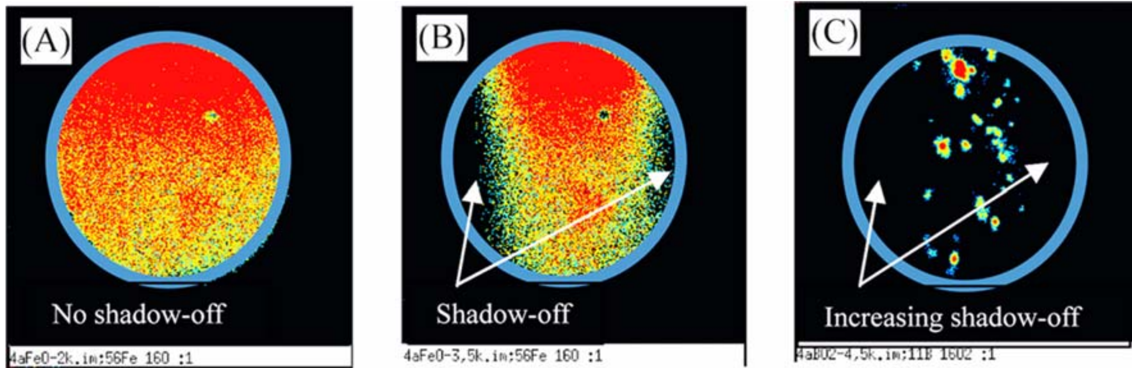

Fig. 6. The field of view shadow-off in RAE ion image at different mass resolutions of (A) MR 2,000 and (B) MR 3,500, and (C) MR 4,500.

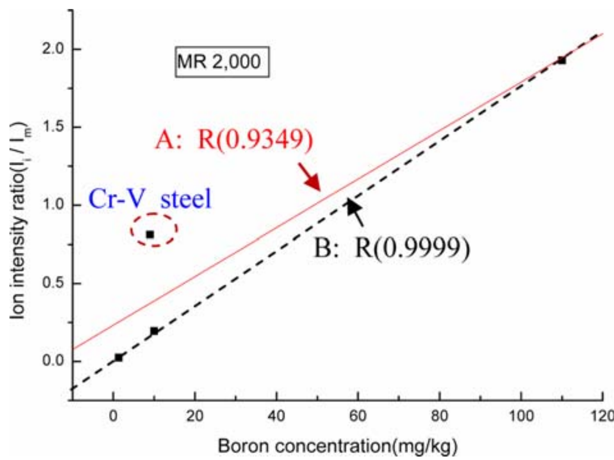

Fig. 7. Relationship between secondary ion intensity ratio ($^{11}B^{16}O_2$/$^{56}Fe^{16}O$) and boron concentration for the iron and steel samples. Measurement was carried out by retrospective depth profile (MR 2,000). The red solid line "A" represents correlation coefficient, R including outlier Cr-V steel. The black broken line "B" represents the correlation coefficient, R excluding the outlier Cr-V steel.

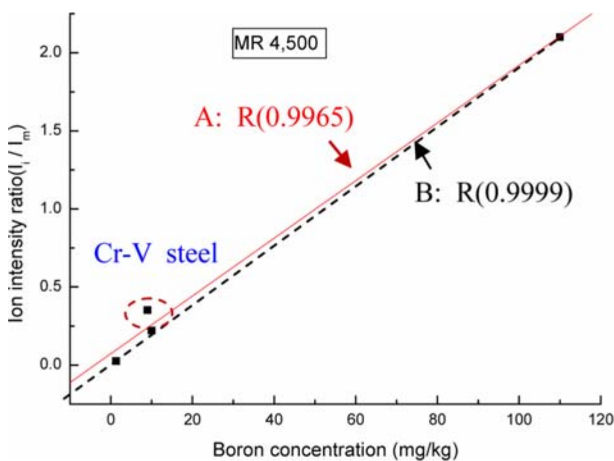

Fig. 8. Relationship between secondary ion intensity ratio ($^{11}B^{16}O_2$/$^{56}Fe^{16}O$) and boron concentration for the iron and steel samples. Measurement was carried out by raster depth profile (MR 4,500). The red solid line "A" represents correlation coefficient, R including the outlier Cr-V steel. The black broken line "B" represents correlation coefficient, R excluding the outlier Cr-V steel.

num concentration is 7 to 80 ppm.

3.2.2. RSF

Impurity atom density can also be quantified by the following equation (2) [11]. An RSF is a conversion factor of secondary ion intensity to atom density.

$$\rho_i = \frac{I_i}{I_m} RSF \quad (2)$$

where ρ_i is the impurity atom density in *atoms*/cm^3, I_i is the secondary ion intensity of impurity in cps, I_m is the secondary intensity of matrix in cps, and RSF in *atoms*/cm^3. The impurity atom density ρ_i of the Cr-V steel can be obtained as follows.

$$\rho_i(atoms/\mathrm{cm}^3) = \frac{at.wt_m \times 9ppm \times \rho_m(atoms/cm^3)}{at.wt_i}$$

$$= \frac{55.847}{10.81} \times 9 \times 8.47E16 atoms/\mathrm{cm}^3$$

$$= 3.9382E18 atoms/\mathrm{cm}^3$$

Determination of the RSF from a known impurity atom density can be made by rearranging the equation (2).

$$\mathrm{RSF} = \rho_i \frac{I_m}{I_i} \quad (3)$$

The RSF of Cr-V steel can be calculated by using the ρ_i in equation (3).

$$\mathrm{RSF} = 3.9382E18 atoms/\mathrm{cm}^3 \; \frac{2.58E3cps}{2.09E3cps}$$

$$= 4.8615E18 atoms/\mathrm{cm}^3$$

The RSF of the test samples are calculated from their relevant retrospective depth profiles or raster depth profiles and summarized in Table 4. Figure 9 shows the variation of the RSF for (A) boron and (B) carbon as a function of the concentration obtained at different mass resolution. The relative standard deviation (RSD) of the RSF_B by retrospective depth profile (RAE image: MR 2,000) was ±21.5 %,

Table 4. Comparison of calculated RSF_B, RSF_C, at different conditions

Test Sample (Matrix)	Retrospective depth profile (MR 2,000)		Raster depth profile (MR 4,500)
	RSF_B (atoms/cm^3)	RSF_C (atoms/cm^3)	RSF_B (atoms/cm^3)
Cr-V steel	4.86E18	2.13E19	1.12E19
High carbon steel	2.49E19	2.14E22	2.29E19
Electrolytic iron	2.26E19	1.56E20	2.13E19
Stainless steel	2.24E19	8.05E20	1.98E19

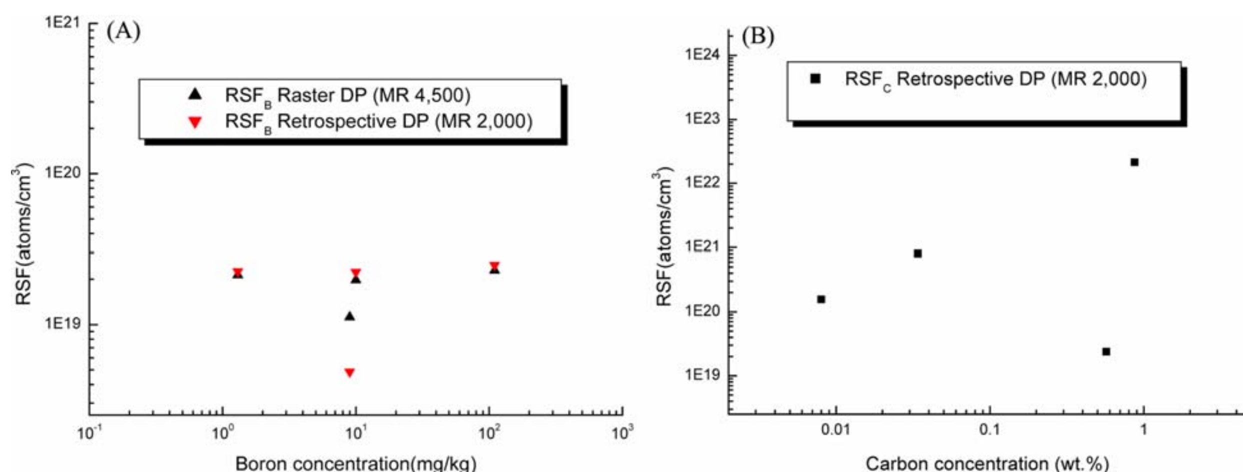

Fig. 9. Variation of RSFs as a function of concentration at different analysis conditions for (A) Boron and (B) Carbon.

Table 5. Reproducibility of the intensity measurements in retrospective depth profile (A) and raster depth profile (B)

(A) Retrospective Depth profile (MR 2,000)		I_i:$^{11}B^{16}O_2$ (cps)	I_m:$^{56}Fe^{16}O$ (cps)	I_i/I_m	Mean	SD	RSD (%)
Cr-V steel	1st point	1.61E3	2.86E3	0.563			
	2nd point	1.46E3	2.74E3	0.533	0.52	0.039189	±3.76
	3rd point	1.36E3	2.93E3	0.469			
High carbon steel	1st point	3.27E3	2.68E3	1.22			
	2nd point	4.67E3	2.78E3	1.68	1.43	0.19066	±6.68
	3rd point	3.75E3	2.72E3	1.38			
Electrolytic iron	1st point	5.53E1	2.49E3	0.0222			
	2nd point	5.83E1	2.50E3	0.0233	0.021	0.00242	±5.74
	3rd point	4.98E1	2.81E3	0.0177			
Stainless steel	1st point	2.50E2	2.72E3	0.0919			
	2nd point	3.63E2	2.53E3	0.1430	0.123	0.02239	±9.1
	3rd point	3.16E2	2.36E3	0.1340			

*Analysis conditions are the same in Table 2.

(B) Raster Depth profile (MR 4,500)		I_i:$^{11}B^{16}O_2$ (cps)	I_m:$^{56}Fe^{16}O$ (cps)	I_i/I_m	Mean	SD	RSD (%)
Cr-V steel	1st point	5.08E3	1.44E4	0.352			
	2nd point	5.30E3	1.40E4	0.379	0.37	0.01271	±1.72
	3rd point	5.28E3	1.39E4	0.380			
High carbon steel	1st point	2.40E4	1.14E4	2.11			
	2nd point	3.54E4	1.40E4	2.53	2.16	0.26911	±6.22
	3rd point	2.65E4	1.41E4	1.88			
Electrolytic iron	1st point	3.57E2	1.34E4	0.0266			
	2nd point	6.55E2	1.49E4	0.0440	0.0311	0.00909	±14.6
	3rd point	2.92E2	1.27E4	0.0230			
Stainless steel	1st point	1.34E3	6.07E3	0.2210			
	2nd point	1.94E3	1.13E4	0.1720	0.147	0.07278	±24.8
	3rd point	7.80E2	1.63E4	0.0479			

*Analysis conditions are slightly different from those in Table 2.

whereas it was ±12% (that is, about half of the former) by raster depth profile (MR 4,500) because of the high mass resolution reducing the interference of aluminum, as mentioned in Section 3.2.1. The RSD of RSF_B without the outlier Cr-V sample, was ±2.43% by retrospective depth profile and ±2.97% by raster depth profile, respectively. In the meantime, the RSD of the RSF_C (B) obtained using a mass resolution of 2,000 was ± 81.6%, and this value is too large to accept as the useful RSF. It is surmised that the detected single atomic ion species of ^{12}C and ^{56}Fe are not entirely representative of the matrix composition. This is due to the strong matrix effect of the quite different microstructure of the iron and steel sample, as shown in Fig. 1. It was reported that the choice of reference element makes a difference up to an order of magnitude 4 in RSF for the different matrix elements [12].

3.2.3. Reproducibility

The type of analysis modes could affect the quantification reliability, so it is necessary to examine the reproducibility of the RAE mode and raster depth profile mode. To do this, measurements at different positions were made three times for all test samples (see Table 5). The data (A) for RAE mode (retrospective depth profile: MR 2,000) was obtained with slightly different analysis conditions from Table 2, but the data (B) for raster depth profile mode (MR 4,500) was obtained with the same analysis conditions in Table 2. The RSD of the data (A) shows less than ±10% and the RSD of data (B) shows a maximum of about ±25% for stainless steel. This is due mainly to the poor transmission of high mass resolution for the raster depth profile. Low count rates enlarged the statistical influences to the relative deviation value. It was reported that the transmission remains unchanged at 40% up to the MR 1,000, but it dramatically drops to 8% at MR 4,000 in the CAMECA IMS 5f instrument [13]. In spite of the poor transmission of MR 4,500, the RSD of Cr-V steel (0.24% Al) was better (±1.72) than the RSD (±3.76) obtained by the high transmission of MR 2,000. This evidence suggests that the aluminum of 0.24 wt% in steel matrix had a decisive effect on the secondary cluster ion intensity of $^{11}B^{16}O_2$.

4. CONCLUSIONS

Based on the calibration curve method, we suggest that it is possible to quantify the trace boron concentration in the range of 1 ppm to 100 ppm for iron and steel from an RAE image. One prerequisite for this is that the sample should have a limited amount of aluminum, that is, less than 100 wt. ppm. The available mass resolution in RAE mode is limited by MR 2,000, and it is not sufficient to eliminate the aluminum interference for an aluminum content of more than 0.24 wt% in boron added iron and steel. It is demonstrated that the detection of the secondary impurity cluster ion of $^{11}B^{16}O_2$ and matrix cluster ion of $^{56}Fe^{16}O$ as a reference was a good trial to reduce the matrix effect. The correlation coefficient of the calibration curve improved from 0.9349 to 0.9996 and the RSD of the RSF_B improved from ±21.5% to ±12% by employing MR 4,500 in raster depth profile. For the quantification of three samples containing less than 100 ppm of aluminum, the RSD of the RSF_B could be decreased down to ±2.43% by using MR 2,000 in retrospective depth profile. Increasing mass resolution leads to a loss of the reproducibility due to the poor transmission. The average reproducibility of the experiments were ±6.3% for RAE mode and ±12.26% for raster depth profile with MR 4,500, respectively. In conclusion, the method using SIMS direct RAE image can be applied to the determination of trace born concentration in the wide range of Al, C, Si, Mn, P, S, Ni, and Cr alloyed iron and steel. It is noted that the SIMS data can be obtained under optimum conditions with a less than ±2% error in reproducibility and ±10% error in accuracy [14].

ACKNOWLEDGMENTS

The authors would like to thank Jeffrey R. Shallenberger, Evans Analytical Group, Massachusetts & New Jersey, USA for the thoughtful discussion. This research was supported in part by the Korean Ministry of Commerce, Industry and Energy.

REFERENCES

1. H. N. Migeon, F Saldi, Y. Gao, M. Schumacher, *Int. J. Mass Spectrometry and Ion process*. **143**, 51 (1995).
2. S. G. Ostrowski, M. E. Kurczy, T. P. Roddy, N. Winograd, and A. G. Ewing, *Anal. Chem*. **79**, 3554 (2007).
3. J. L. S. Lee, I. S. Gilmore, and M. P. Seah, *Sur. Interface Anal*. **40**, 1 (2008).
4. T. Zacharia, *ICMCJP*, pp. 153-160, American Welding Society, Orlando, Florida (1993).
5. S. K. Banerji and J. E. Morral, *Conf. Proc*. pp. 1-215, TMS-AIME, Warrendale, PA, USA (1980).
6. I.-S. Chung and S.-G. Cho, *J. Kor. Inst. Met. Mater*. **31**, 1191 (1993).
7. F. B. Pickering, *Physical Metallurgy and the design of steels*, pp. 1-275, App. Sci., UK (1978).
8. R. Stuck, J. P. Ponpon, A. Benninghoven, A. M. Huber, and H. W. Werner, *Secondary Ion Mass Spectrometry SIMS VI*, p. 507, Wiley, New York (1988).
9. P. Laty, D. Seethanen, and F. Degrev, *Surf. Sci*. **85**, 353 (1979).
10. K. Wittmaack, Int. J. Mass Spectrometer, *Ion Phys*. **17**, 39 (1975).
11. R. G. Wilson, F. A. Stevie, and C. W. Magee, *Secondary Ion Mass Spectrometry A Practical Handbook*, 2.4.1, John

Wiley & Sons, New York (1989).
12. R. G. Wilson, F. A. Stevie, and C. W. Magee, *Secondary Ion Mass Spectrometry A Practical Handbook*, 3.3, John Wiley & Sons, New York (1989).
13. H. N. Migeon, F Saldi, Y. Gao, and M. Schumacher, *Int. J. Mass Spectrometry and Ion process*. **143**, 51 (1955).
14. R. G. Wilson, F. A. Stevie, and C. W. Magee, *Secondary Ion Mass Spectrometry A Practical Handbook*, 3.1.1, John Wiley & Sons, New York (1989).